New insight into phase behavior and permeability of skin lipid models based on sphingosine and phytosphingosine ceramides

L.E. Uche, G.S. Gooris, C.M. Beddoes, J.A. Bouwstra*

Division BioTherapeutics, Leiden Academic Centre for Drug Research, Leiden University, Netherlands

ABSTRACT

The intercellular lipid matrix of the *stratum corneum* (SC), which consist mainly of ceramides (CERs), free fatty acids and cholesterol, is fundamental to the skin barrier function. These lipids assemble into two lamellar phases, known as the long and short periodicity phases (LPP and SPP respectively). The LPP is unique in the SC and is considered important for the skin barrier function. Alterations in CER composition, as well as impaired skin barrier function, are commonly observed in diseased skin, yet the understanding of this relationship remains insufficient. In this study, we have investigated the influence of non-hydroxy and α-hydroxy sphingosine-based CERs and their phytosphingosine counterparts on the permeability and lipid organization of model membranes, which were adjusted in composition to enhance formation of the LPP. The permeability was compared by diffusion studies using ethyl-p-aminobenzoate as a model drug, and the lipid organization was characterized by X-ray diffraction and infrared spectroscopy. Both the sphingosine- and phytosphingosine-based CER models formed the LPP, while the latter exhibited a longer LPP repeat distance. The ethyl-p-aminobenzoate flux across the sphingosine-based CER models was higher when compared to the phytosphingosine counterparts, contrary to the fact that the α-hydroxy phytosphingosine-based CER model had the lowest chain packing density. The unanticipated low permeability of the α-hydroxy phytosphingosine-based model is probably associated with a stronger headgroup hydrogen bonding network. Our findings indicate that the increased level of sphingosine-based CERs at the expense of phytosphingosine-based CERs, as observed in the diseased skin, may contribute to the barrier function impairment.

1. Introduction

The skin is a large multilayered organ with the primary function of protecting the body from an influx of dust, pathogens, chemicals, ultraviolet radiation and other unwanted substances in the external environment, while also preventing the excessive loss of fluids from the body [1]. The outermost layer of the skin, the *stratum corneum* (SC), is fundamental to the skin barrier function [2,3]. It consists of keratin-filled dead cells, referred to as corneocytes, embedded in a highly organized lipid matrix [4]. The cornified cross-linked protein envelope encapsulates the corneocytes and renders them highly impermeable. Consequently, the tortuous intercellular pathway occupied by the lipid matrix is the preferred pathway for exogenous substance penetration through the skin [5,6]. Thus, knowledge of the lipid composition and organization is crucial to understand the skin barrier function.

The major lipid classes in the SC are ceramides (CERs), cholesterol (CHOL) and free fatty acids (FFAs) [7–11]. These lipids are present in an approximately equimolar ratio in the human SC. As detected by X-ray diffraction, the SC lipids are assembled into either one of two co-existing crystalline lamellar phases with repeat distances of ~13 nm and ~6 nm referred to as the long and the short periodicity phases (LPP and SPP) respectively [12–14]. Within the lipid lamellae, the lipids can further assemble into various phases with distinct packing densities including the orthorhombic, hexagonal and liquid/fluid phases. At physiological temperature, these lipids adopt predominantly a dense orthorhombic lateral packing, while a subpopulation of the lipids arranges to form lesser densely packed phases including the hexagonal and disordered liquid phase [15–18]. Both the lamellar organization and the lateral packing of the SC lipids are important for the skin barrier function [19].

The CERs, unlike the other major SC lipid classes, show great diversity in their headgroup architecture. Currently, eighteen CER subclasses have been identified in human SC [20–27]. Several studies have investigated the phase behavior of SC lipid mixtures prepared with isolated CERs, in order to gain insight into the processes and factors underlying the skin barrier function [28–30]. CERs isolated from skin
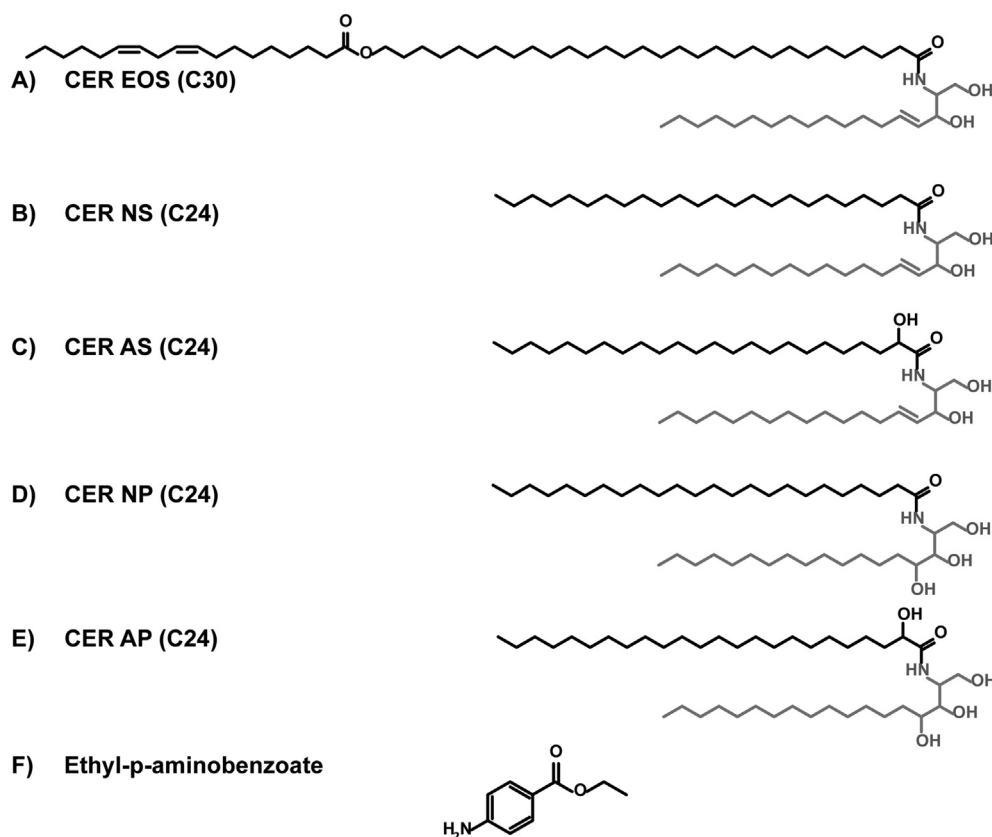

Fig. 1. Molecular structure of the CER subclasses and ethyl-p-aminobenzoic acid used in the study. The CERs consist of a fatty acid acyl chain {non-hydroxylated [N], α-hydroxylated [A] or ω-hydroxylated [O]} linked by an amide bond to a sphingoid base {sphingosine [S], or phytosphingosine [P] with 18 carbon atoms}. A) N-(30-Linoleoyloxy-triacontanoyl)-sphingosine: a linoleate esterified to an ω-hydroxylated acyl chain [EO], with a chain length of 30 carbon atoms (C30) linked to a [S] base, referred to as CER EOS (C30); B) N-(tetracosanoyl)-sphingosine: a [N] acyl chain (C24) linked to a [S] base, referred to as CER NS (C24); C) N-(2R-hydroxy-tetracosanoyl)-sphingosine: an [A] acyl chain (C24) linked to a [S] base, referred to as CER AS (C24); D) N-(tetracosanoyl)-phytosphingosine: a [N] acyl chain (C24) linked to a [P] base, referred to as CER NP (C24); and E) D-(2R-hydroxy-tetracosanoyl)-phytosphingosine: an [A] acyl chain (C24) linked to a [P] base referred to as CER AP (C24). The [P] based CERs, NP and AP contain a C4 hydroxyl group on the base chain while [A] based CERs, AS and AP contain a hydroxyl group on the fatty acid moiety. The CER fatty acid acyl chain and sphingoid base are depicted in black and grey respectively. F) Molecular structure of ethyl-p-aminobenzoate (*E*-PABA) used as a model drug for the permeability studies.

lipids can form the characteristic LPP and SPP only when mixed with CHOL [31], while the further addition of FFAs increases the packing density [32]. Alternatively, synthetic lipid model systems can range from simple ternary component mixtures [33–35] to complex mixtures that contain a greater number of components [36–38] and have been utilized to study the contributions of the major lipid classes and subclasses to SC lipid organization. With the use of these models, the CER EOS subclass, belonging to the group of ester-linked ω-hydroxy CERs (Fig. 1A), has been identified as crucial for the formation of the LPP [32,39–41]. The LPP is unique in the SC, which indicates its importance for the integrity of the skin barrier [42]. To investigate the influence of SC lipid composition and organization to barrier function, several studies have examined the influence of CER subclasses on the permeability of model SC membranes [42–46]. However, most of these studies were carried out in models containing either a single CER or a mixture of CERs, while lacking ester-linked ω-hydroxy CERs, so that the LPP was not formed. For a comprehensive understanding of the relationship between CER composition, lipid organization and barrier function, it is necessary to investigate the influence of the CER headgroup structure on the formation of the LPP, molecular interactions and lipid chain packing, as well as how these interactions can influence the SC lipid barrier function in models organized in the LPP. This is of special importance as variation in CER subclass composition has been reported in several diseased skin conditions including; atopic dermatitis [26] and psoriasis [47], which express among other anomalies, a reduction in ester-linked ω-hydroxy CERs level and thus LPP formation, and an increase in sphingosine-based CER level at the expense of phytosphingosine-based CERs.

In the current work, we aimed to determine the influence of sphingosine- and phytosphingosine-based CERs on the permeability, lamellar organization, phase transitions, headgroup interactions, chain conformational ordering, lateral packing and mixing properties in LPP lipid model systems. The level of CER EOS (molecular architecture, see Fig. 1) was increased to 40 mol% to avoid the formation of the SPP in

the lipid model systems [48,49]. The significance of our findings to impaired skin barrier function in inflammatory skin disease is discussed.

2. Materials and method

2.1. Materials

Molecular structure of the five synthetic CER subclasses used to prepare the model mixtures are displayed in Fig. 1A–E. The synthetic CERs were kindly provided by Evonik (Essen, Germany). The CERs were of ≥90% purity. The FFAs, Ethyl-p-aminobenzoate referred to as *E*-PABA (Fig. 1F), CHOL and acetate buffer salts were purchased from Sigma- Aldrich Chemie GmbH (Schnelldorf, Germany). The perdeuterated FFAs (DFFAs) with chain lengths of C18 and C20 were obtained from Cambridge Isotope Laboratories (Andover, Massachusetts). The DFFAs with chain lengths of C16 and C22 were obtained from Larodan (Malmö, Sweden). The DFFA with a chain length of C24 was obtained from Arc Laboratories B.*V*. (Apeldoorn, The Netherlands). All organic solvents were purchased from Labscan Ltd. (Dublin, Ireland). All analytical solvents were HPLC grade or higher. The nucleopore polycarbonate filter disks, 0.05 μm pore size were purchased from Whatman (Kent, UK).

2.2. Preparation of the model lipid mixtures

SC lipid models were prepared as equimolar mixtures of CER, CHOL, and FFAs. The CER fraction comprised of CER EOS (40 mol% of the total CER fraction) and either CER NS, CER AS, CER NP or CER AP (60 mol% of the total CER fraction). The FFA content comprised of FFAs with the following composition: C16, C18, C20, C22 and C24 at relative molar percentages of 1.8, 4.0, 7.6, 47.8 and 38.8 respectively, a composition adapted from the FFA composition in the SC [50]. The resulting lipid models, whose compositions are presented in Table 1, are

Table 1
Composition of the various models used in the study.

Lipid model name	Composition and molar ratio (1:1:1)
CER EOS-NS	CER EOS(C30) 40% + NS(C24) 60%: CHOL: FFAs
CER EOS-AS	CER EOS(C30) 40% + AS(C24) 60%: CHOL: FFAs
CER EOS-NP	CER EOS(C30) 40% + NP(C24) 60%: CHOL: FFAs
CER EOS-AP	CER EOS(C30) 40% + AP(C24) 60%: CHOL: FFAs
CER EOS-NS-D	CER EOS(C30) 40% + NS(C24) 60%: CHOL: DFFAs
CER EOS-AS-D	CER EOS(C30) 40% + AS(C24) 60%: CHOL: DFFAs
CER EOS-NP-D	CER EOS(C30) 40% + NP(C24) 60%: CHOL: DFFAs
CER EOS-AP-D	CER EOS(C30) 40% + AP(C24) 60%: CHOL: DFFAs

denoted by CER EOS-NS, CER EOS-NP, CER EOS-AS, and CER EOS-AP. Additional models were prepared in which FFAs were replaced by their deuterated counterparts, denoted by CER EOS-NS-D, CER EOS-NP-D, CER EOS-AS-D, and CER EOS-AP-D.

2.3. Preparation of SC model membranes for permeability studies

To prepare the SC model membranes, 0.9 mg of the appropriate lipid composition was dissolved in 200 µl hexane:ethanol (2:1) solution, to a final concentration of 4.5 mg/ml. The solution was sprayed over an area of 10 × 10 mm, on a nucleopore polycarbonate filter disk with 0.05 µm pore size (Whatman, Kent, UK), using a Linomat IV device with an extended y-axis arm (Camag, Muttenz, Switzerland) under a gentle stream of nitrogen. Spraying rate was set at 14 µl/s and an approximate distance of 1 mm was maintained between the nozzle and the spraying surface. The samples were equilibrated for 10 min at 85 °C, which was sufficient to ensure that the lipid mixtures had fully melted and then gradually cooled to room temperature. The heating and cooling cycle was repeated once more.

2.4. Permeability studies

In vitro permeation studies were performed using Permegear in-line diffusion cells (Bethlehem PA, USA) with a diffusion area of 0.28 cm². The model membranes prepared with the various lipid mixtures were mounted in the diffusion cells and hydrated for an hour with the acceptor phase consisting of phosphate buffered saline (PBS 0.1 M solution: NaCl, Na$_2$HPO$_4$, KH$_2$PO$_4$ and KCl in milli-Q water with a concentration of 8.13, 1.14, 0.20 and 0.19 g/l respectively) at pH 7.4 prior to the experiment. Before use, the PBS was filtered and degassed for 30 min under vacuum to remove the dissolved air. As a model drug, E-PABA was used, as it results in acceptor phase samples with sufficiently high concentrations that are measurable with the UPLC. The donor compartment was filled with 1400 µl of E-PABA in acetate buffer (pH 5) at a saturated concentration of 0.65 mg/ml. This concentration was used to enable the maximum thermodynamic activity. The acceptor phase was perfused at a flow rate of about 2 ml/h with an Ismatec IPC pump (IDEX Health & Science, Germany) through an in-line degasser (Biotech, Sweden) to remove air bubbles that may form during the experiment. The acceptor phase was stirred with a tico 731 magnetic stirrer (Hengstler, Germany) at 120 rpm. The experiment was performed under occlusive conditions, by closing the opening of the donor compartment with an adhesive tape. The temperature of the membranes was maintained at 32 °C. The acceptor fluid was collected over 15 h at 1-hour intervals. At the end of the diffusion study, the volume per collected fraction of PBS was determined by weight and the concentration of E-PABA was determined by UPLC (see below). During the steady-state conditions, the permeation of E-PABA across the model membrane can be described by Fick's first law of diffusion:

$$J_{ss} = \frac{K.\,D.\,C_d}{h.}$$

J_{ss} represents the steady-state flux of E-PABA across the model

membrane (µg/cm²/h), while D is the diffusion coefficient of E-PABA in the model membrane (cm²/h). K is the partition coefficient between the donor compartment and the lipid membrane. C_d is the drug concentration (µg/cm³), and h is the pathway length in the model membrane (cm). Permeation of multiple samples of each composition was analyzed, $n \geq 4$. The steady-state flux values were calculated at a time interval between the 9th and 15th hour from the plots of E-PABA flux values.

2.5. Ultra high performance liquid chromatography (UPLC)

The analysis of E-PABA was carried out using Acquity UPLC systems (Waters Co., Milford, MA, USA). The Waters' Acquity UPLC systems consisted of a quaternary solvent manager (a high-pressure pump), tunable ultraviolet/visible absorbance detector controlled by MassLynx software application, and sample manager with flow-through needle. Specialized Acquity UPLC column packed with 1.7 µm, bridged, ethyl siloxane, hybrid particles, was used as the stationary phase. The column temperature was set at 40 °C. The mobile phase used for the UPLC analysis contained mixtures of 0.1% trifluoroacetic acid in acetonitrile: milli-Q water at 40:60 (v/v) ratio. The flow rate of the mobile phase was set at 1 ml/min. 10 µl of sample was injected on the column. A UV-detection wavelength of 286 nm was used for the detection of E-PABA. MassLynx software was used for the acquisition of data in chromatogram peaks resulting from the permeation samples. All UPLC data were analyzed and processed using MassLynx and TargetLynx software V4.1 SCN951 (Waters Co., Milford, USA).

The analytical method was validated as per ICH (International conference on harmonization) guidelines with respect to linearity, precision, limit of detection (LOD) and limit of quantification (LOQ) [51]. Calibration standards were prepared by serial dilutions of stock solution in order to evaluate the relationship between the area under the curve and the concentration of E-PABA. The solutions were prepared in 1:1 solution of methanol and milli-Q water. The linearity of the relationship was evaluated in a concentration range of 0.1–10 µg/ml covering the range of concentrations obtained when analyzing the concentration of E-PABA permeating the model membranes. The calibration curves were obtained using ordinary least square linear regression and the linearity was confirmed with the R² values. A series of calibration samples were run together with the samples to quantify E-PABA. To assess the system precision, E-PABA standard solution was prepared and six replicate injections were injected into the UPLC system and the percentage relative standard deviation (% RSD) was determined. The limit of quantification (LOQ) and limit of detection (LOD) were used to evaluate the quantitative performance and sensitivity of the method for E-PABA analysis [51,52].

2.6. Sample preparation for FTIR studies

1.5 mg of the appropriate lipid composition was dissolved in chloroform:methanol (2:1) to a concentration of 7.5 mg/ml and sprayed over an area of 10 × 10 mm² on an AgBr window using a Linomat IV device (Camag, Muttenz, Switzerland) with an extended y-axis arm and equilibrated as described earlier (Section 2.3). The samples were equilibrated at 85 °C. A higher equilibration temperature of 95 °C was used for CER EOS-NP-D and CER EOS-AP-D mixtures in order for the lipids to fully melt. Finally, the samples were hydrated in deuterated acetate buffer (pH 5.0) and incubated at 37 °C for at least 15 h to ensure that the samples were fully hydrated.

2.7. FTIR measurements

FTIR spectra were acquired on a Bio-Rad Excalibur series FTIR spectrometer (Cambridge, MA) equipped with a broad-band mercury cadmium telluride detector, cooled by liquid nitrogen. The sample was continuously dry air purged, starting 30 min prior to data acquisition.
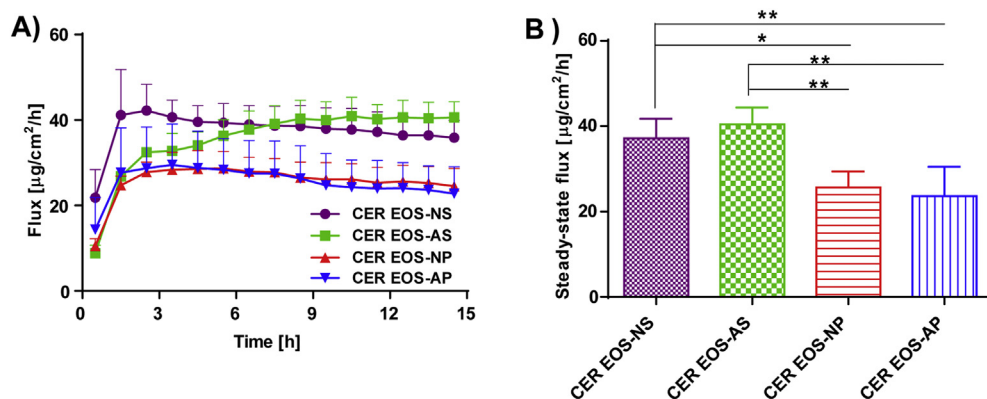
Fig. 2. Permeability of the model membranes. A) The flux of *E*-PABA across the model membranes over 15 h. B) The average steady-state flux of E-PABA across the model membranes (9–15 h). Data presented as the means ± SD, $n \geq 4$. E-PABA steady-state flux was significantly lower in the phytosphingosine-based CER model compared to their sphingosine analogues, [** ($P < 0.01$), * ($P < 0.05$)].

The spectra were generated in the transmission mode by the coaddition of 256 interferograms, collected at $1\,cm^{-1}$ resolution over 4 min. In order to examine the thermotropic phase behavior, the sample was measured between 0 and $100\,°C$ at a heating rate of $0.25\,°C/min$, resulting in a $1\,°C$ temperature rise per recorded spectrum. The spectra were deconvoluted using a half-width of $4\,cm^{-1}$, and an enhancement factor of 1.7. The software used was Agilent resolution pro (Agilent Technologies, Palo Alto CA, USA). Samples were measured over a range of $600–4000\,cm^{-1}$. The CH_2 symmetric stretching modes ($2845–2855\,cm^{-1}$) and CD_2 symmetric stretching modes ($2080–2100\,cm^{-1}$), referred to as ν_sCH_2 and ν_sCD_2 modes respectively, were selected to examine the conformational ordering and phase transition of the lipid chains. The linear regression curve fitting method was used to determine the mid-transition temperature and the transition temperature range, as described elsewhere [53]. The CH_2 ($1462–1473\,cm^{-1}$) and CD_2 ($1085–1095\,cm^{-1}$) scissoring modes referred to as δCH_2 and δCD_2 modes respectively were analyzed to monitor the lateral packing and mixing properties of the lipid chains. The frequencies of the CER amide I ($1610–1690\,cm^{-1}$) and amide II ($1510–1560\,cm^{-1}$) modes were analyzed to investigate the headgroup interactions and peak positions determined from the second derivative spectra. Multiple measurements of the samples were made, $n \geq 2$.

2.8. Sample preparation for X-ray diffraction studies

Sample preparation was similar to that described for FTIR studies. 1.0 mg of lipids in chloroform:methanol (2:1) solution was sprayed on a mica window at a concentration of 7.5 mg/ml. The samples were equilibrated for 10 min at $85\,°C$ and were subsequently measured both dry and fully hydrated. The lipid organization was not influenced by the number of equilibrations (either single or double, Fig. S1).

2.9. X-ray diffraction studies

The diffraction measurements were performed at the European Synchrotron Radiation Facility (ESRF, Grenoble) at station BM26B. The small- and wide-angle X-ray diffraction (SAXD and WAXD) patterns were acquired simultaneously. SAXD images were collected using a Pilatus 1M detector with 981×1043 pixels of $172\,\mu m$ spatial resolution while the WAXD patterns were collected using a 300K-W linear Pilatus detector with 1475×195 pixels of $172\,\mu m$ spatial resolution. The spatial calibration of the detectors was performed using silver behenate. The X-ray wavelength was set at 0.1033 nm. The sample-to-detector distances were 2.1 m and 0.308 m for SAXD and WAXD respectively. The samples were mounted in a sample holder with mica windows. Diffraction patterns of the lipid models were acquired at room temperature on two positions, at each position, the samples were measured for 90 s. SAXD was used to determine the long-range ordering in the samples. The scattering intensity (I) was measured as a function of the scattering vector q. The latter is defined as $q = (4\pi \sin \theta)/\lambda$,

where θ is the scattering angle and λ is the wavelength. From the positions of a series of equidistant peaks (q_n), the periodicity of a lamellar phase was calculated using the equation $d = 2n\pi/q_n$ in which n is the order of the diffraction peak. The one-dimensional intensity profiles used in these calculations were obtained by the reduction of the 2D SAXD pattern from Cartesian (x,y) to polar (ρ,θ) coordinates and integrated over an θ range. WAXD was used to obtain the diffraction patterns related to the lateral packing of lipids. Each sample was measured at least twice.

2.10. Data analysis

One-way ANOVA with Bonferroni's multiple comparison test was performed to analyze the permeability studies' data. The significance level for rejection of null hypothesis was set at $P < 0.05$ (*), $P < 0.01$ (**), $P < 0.001$ (***) and $P < 0.0001$ (****).

3. Results

3.1. Phytosphingosine-based CER model membranes exhibit higher barrier capability than the sphingosine-based CER model membranes

The permeability of *E*-PAPA through the model membranes was evaluated by in-vitro permeation studies. E-PABA was analyzed by means of the UPLC method. The calibration curve R^2 value was 0.9989 ± 0.0023 indicating excellent linearity. For assessment of the system precision, the RSD for the peak area obtained from six replicate injections was $9248.7 \pm 0.1\%$ (acceptance limit of NMT 2.0%) demonstrating high repeatability. The LOD and LOQ values were 0.10 ± 0.01 ng/ml and 0.51 ± 0.02 ng/ml respectively, demonstrating the high sensitivity and quantitative performance of the UPLC method for *E*-PABA analysis.

The E-PABA flux profiles are displayed in Fig. 2A. The bars of steady-state fluxes are shown in Fig. 2B, while the values are reported in Table 2. The steady-state flux of *E*-PABA was significantly lower in

Table 2
The E-PABA steady-state flux across the model membranes with their standard deviation, the midpoint temperatures of the orthorhombic-hexagonal phase transition ($T_{M,OR-HEX}$) and hexagonal-liquid phase transition ($T_{M,HEX-LIQ}$), the widths of the orthorhombic-hexagonal ($T_{W,OR-HEX}$) and hexagonal-liquid transition ($T_{W,HEX-LIQ}$).

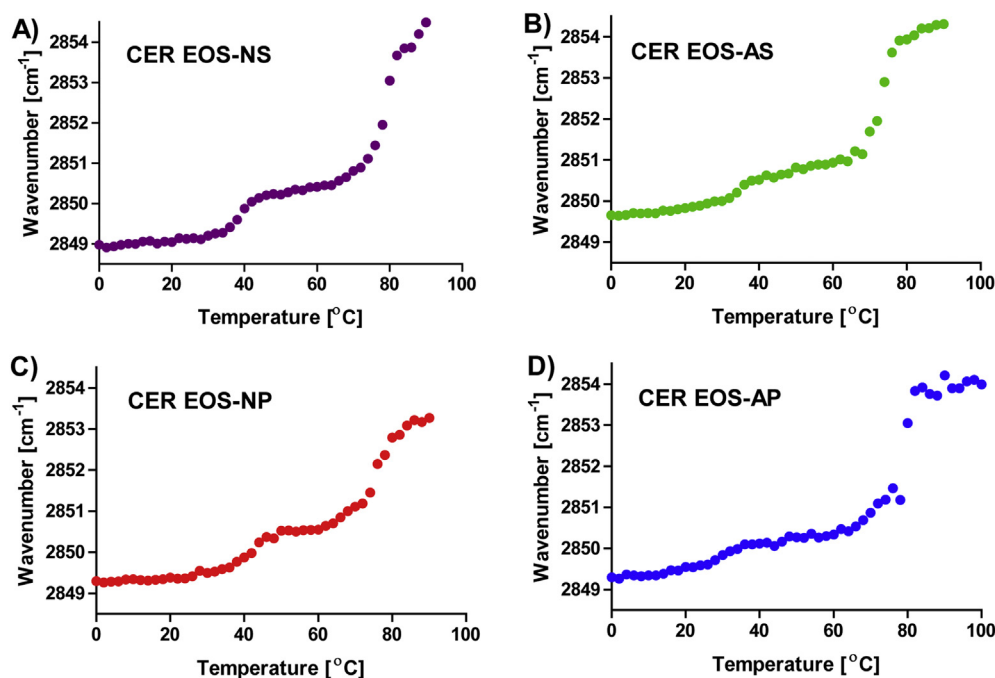| Lipid model	Steady-state flux (µg/cm²/h)	$T_{M,OR-HEX}$ (°C)	$T_{W,OR-HEX}$ (°C)	$T_{M,HEX-LIQ}$ (°C)	$T_{W,HEX-LIQ}$ (°C)
CER EOS-NS	37.1 ± 4.5	38.5 ± 0.8	8.3	74.7 ± 3.2	9.1
CER EOS-AS	40.4 ± 3.9	34.5 ± 0.3	8.5	73.3 ± 0.3	8.1
CER EOS-NP	25.7 ± 3.8	41.7 ± 1.8	12.8	73.7 ± 1.5	19.4
CER EOS-AP	23.7 ± 6.8	28.7 ± 0.3	9.4	78.5 ± 1.6	18.7

Fig. 3. Thermotropic response of the v_sCH$_2$ modes of the lipid models. The v_sCH$_2$ modes of all models showing frequencies below 2850 cm^{-1} at 10 °C, orthorhombic-hexagonal phase transition between 30 and 50 °C and hexagonal-liquid phase transition between 70 and 90 °C.

the phytosphingosine-based CER models compared to the sphingosine-based CER counterparts. In contrast, no significant difference in the *E*-PABA steady-state flux was observed between models prepared with non-hydroxy fatty acid based CERs and with their α-hydroxy fatty acid counterparts.

3.2. Models prepared with phytosphingosine-based CERs undergo a gel to liquid phase transition over a wider temperature range compared to models prepared with sphingosine-based CERs

To probe the factors that dictate the difference in the observed permeability rates, the lateral lipid organization was examined by FTIR spectroscopy. The conformational ordering in the lipid models was examined using the v_sCH$_2$ frequencies. A v_sCH$_2$ frequency below 2850 cm^{-1} indicates the presence of primarily ordered lipid chains typical in a hexagonal and/or orthorhombic lateral packing [54]. The thermotropic response of the v_sCH$_2$ mode of the various lipid models are presented in Fig. 3. The v_sCH$_2$ frequencies in the spectra of the CER EOS-NS, CER EOS-AS, CER EOS-NP, and CER EOS-AP at 10 °C appear at 2849.0, 2849.7, 2849.3 and 2849.3 cm^{-1} respectively, indicative of a high conformational hydrocarbon chain ordering in all of the models. When gradually increasing the temperature, the v_sCH$_2$ frequencies also gradually increased. The first shift in v_sCH$_2$ frequency, of approximately 1 cm^{-1}, indicates an orthorhombic-hexagonal phase transition. Differences in the shift magnitude are observed between the models. The v_sCH$_2$ frequency shift is more pronounced in the models containing non-hydroxy fatty acid based CERs compared to their α-hydroxy fatty acid based counterparts. When increasing the temperature further, a second major transition from a hexagonal to the liquid phase is observed. In the v_sCH$_2$ curve, this is seen as a wavenumber shift of 3–4 cm^{-1}, which in our samples occur between 70 and 90 °C. In the sphingosine-based CER models, the hexagonal-liquid phase transitions occurred with an immediate sharp rise in wavenumber over a shorter temperature range (Fig. 3A and B). In contrast, in the phytosphingosine-based CER models, the hexagonal-liquid phase transition commenced gradually with a wavenumber increase of ~0.5 cm^{-1} over 10 °C, followed by a sharper rise in v_sCH$_2$ wavenumber. When comparing models prepared with CERs, which differ in their fatty acid acyl chain e.g. CER

NS and AS, there is no difference between the hexagonal-liquid phase transition profile. From these thermotropic response curves, the midpoint temperatures of the orthorhombic-hexagonal phase transition (T$_{M,OR-HEX}$) and hexagonal-liquid phase transition (T$_{M,HEX-LIQ}$), the temperature widths of the orthorhombic-hexagonal (T$_{W,OR-HEX}$) and hexagonal-liquid transition (T$_{W,HEX-LIQ}$) were calculated. These values are presented in Table 2. The hexagonal-liquid phase transitions occurred over a wider temperature range in the phytosphingosine-based CER models when compared to their sphingosine counterparts. In CER EOS-NS, a comparatively high T$_{M,HEX-LIQ}$ standard deviation was observed as recrystallization occurred to different extents in replicate samples analyzed (see Fig. S2). When focusing on the midrange temperature (T$_M$), the CER EOS-AP had the highest T$_{M,HEX-LIQ}$ indicating increased thermostability.

3.3. CER EOS-AP exhibited the least proportion of orthorhombic packing at skin physiological temperature

When lipid chains adopt a dense orthorhombic lateral packing, two bands are observed in the IR spectrum of the δCH$_2$ mode. This doublet is due to short-range coupling between adjacent hydrocarbon chains of the same isotope and is distinct from the less dense hexagonal packing where only a single peak is observed in the δCH$_2$ mode. The magnitude of the band splitting is indicative of the degree of inter-chain interactions and of the size of the domains with an orthorhombic organization [16,55,56]. The δCH$_2$ mode of the lipid models at 10 °C and 32 °C are provided in Fig. 4A and B respectively. At 10 °C the δCH$_2$ mode of all lipid models are split into two bands centered at 1462 cm^{-1} and 1473 cm^{-1}, signifying orthorhombic packing. The δCH$_2$ mode of CER EOS-AP showed lower intensity peaks compared to the other compositions indicating a lower fraction of hydrocarbon chains in orthorhombic packing. At 32 °C, the δCH$_2$ modes of CER EOS-AP displayed a single broad peak with a weak shoulder indicating significant orthorhombic-hexagonal shift while the δCH$_2$ mode peaks of CER EOS-NS, CER EOS-AS, and CER EOS-NP remained doublets but reduced in peak intensity (Fig. 4B). As the temperature increased, a pronounced reduction in band splitting was obtained in all samples. The components collapse into a single peak at slightly different temperatures indicating
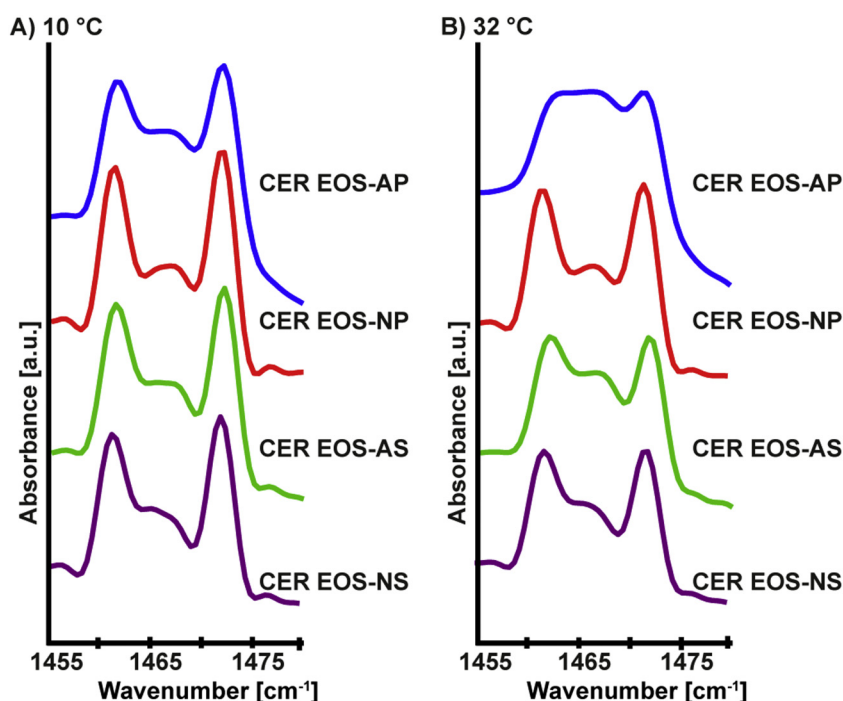
Fig. 4. δCH_2 modes of the lipid models. A) The curves at 10 °C display two distinct bands at approximately 1462 cm^{-1} and 1473 cm^{-1} indicating orthorhombic lateral packing. B) The curve at skin temperature (32 °C).

the transition to a hexagonal packing (Fig. S3).

3.4. The CERs and FFAs undergo order to disorder phase transition in the same temperature range

If the structurally different lipids are fully mixed, the components will have the same melting temperature range. To determine whether the CERs and FFAs had completely mixed, the protiated FFAs were replaced by the DFFAs enabling the protiated CER and DFFA chains to be monitored both individually and simultaneously. The thermotropic response of the $\nu_s CH_2$ and $\nu_s CD_2$ modes of the various lipid models are presented in Fig. 5. In the FTIR spectrum of the CER EOS-NS-D (Fig. 5A), the $\nu_s CD_2$ mode revealed that the hexagonal-liquid phase transition of the deuterated chains commenced at 66 °C. The hexagonal-liquid phase transition of the CER chains also starts at a similar temperature, but the slight reduction in $\nu_s CH_2$ frequencies at 68 °C suggests that the protiated chains had recrystallized, thereby slightly delaying the transition. As the temperature was further increased, the ordered-disordered phase transition of the CER and DFFA chains concluded at the same temperature. A similar phase behavior was shown by CER EOS-AS (Fig. 5B). In the FTIR spectrum of the CER EOS-NP-D (Fig. 5C), the different phase transition temperatures of the CER and DFFA chains suggests the existence of separate CER and DFFA domains. In the FTIR spectrum of CER EOS-AP-D (Fig. 5D), the $\nu_s CD_2$ mode revealed a slight upward shift in wavenumber between 66 °C and 76 °C. At higher temperature, the thermotropic response of the DFFAs and CER chains underwent order to disorder phase transition in the same temperature range indicating mixing of the lipid chains. The hexagonal-liquid phase transition of the DFFA chains in CER EOS-AP-D occurred at a higher temperature than in the other lipid models (Fig. 5E).

3.5. The CERs and FFAs participate in the same orthorhombic lattice at physiological temperature

When deuterated FFA and protiated CER chains participate in the same orthorhombic lattice, the adjacent CD_2 and CH_2 groups, being of different isotopes with different vibrational frequencies, cannot engage

in a short-range coupling. As a consequence, when both isotopes are present in one lattice, only a single peak is observed in δCH_2 and δCD_2 modes while packed in the orthorhombic phase. The δCD_2 mode of the various models and DFFA mixture at 10 °C are displayed in Fig. 6A. The δCD_2 mode from the DFFAs in CER EOS-NS-D, CER EOS-AS-D, and CER EOS-NP-D are split into two bands, indicating coupling of adjacent DFFA chains. In contrast, the δCD_2 mode of CER EOS-AP-D exhibits an additional central peak, likewise observed in the δCH_2 mode at ~1467 cm^{-1} (Fig. S4B), attributed to both a fraction of lipids in a hexagonal phase and the presence of CD_2-CH_2 interaction. The size of the orthorhombic domain formed by the deuterated lipids was evaluated by measuring the magnitude of band splitting in the δCD_2 mode, in the region approximately 1080–1100 cm^{-1} using the spectra collected at 10 °C. The magnitude of the band splitting of pure DFFA mixture was 7.2 cm^{-1}, which represents maximum CD_2-CD_2 peak splitting in a fully deuterated environment. The splitting values measured in the samples were 3.3, 4.1 and 3.9 cm^{-1} for CER EOS-NS-D, CER EOS-AS-D and CER EOS-NP-D respectively. The reduction of the splitting and the shallower minima between the δCD_2 peaks in the spectrum of the various models compared to that of pure DFFA mixture represent reduced CD_2-CD_2 chain interaction and an increased CH_2-CD_2 chain interaction, indicating mixing of the deuterated and protiated chains. Evidently, due to the equimolar ratio of the lipid classes, a fraction of the DFFA chains in the lipid mixtures remain close enough to interact portrayed by the weak splitting. When increasing the temperature, the splitting of the δCD_2 mode of the various models collapse into single peaks (Fig. S4A). The δCD_2 mode of the various models and DFFA mixture at 32 °C are displayed in Fig. 6B. Only one peak or a weak split was detected in the spectra of all models. This may be due to a mixed effect of an increased CD_2-CH_2 interaction and a transition from orthorhombic to hexagonal packing. A similar behavior was displayed by the δCH_2 mode from the CER chains (Fig. S4B).

3.6. CER headgroup interactions differ in the various models

The content of free hydroxyl groups and an amide group enable CERs to act as both hydrogen bond donors and acceptors [57]. To
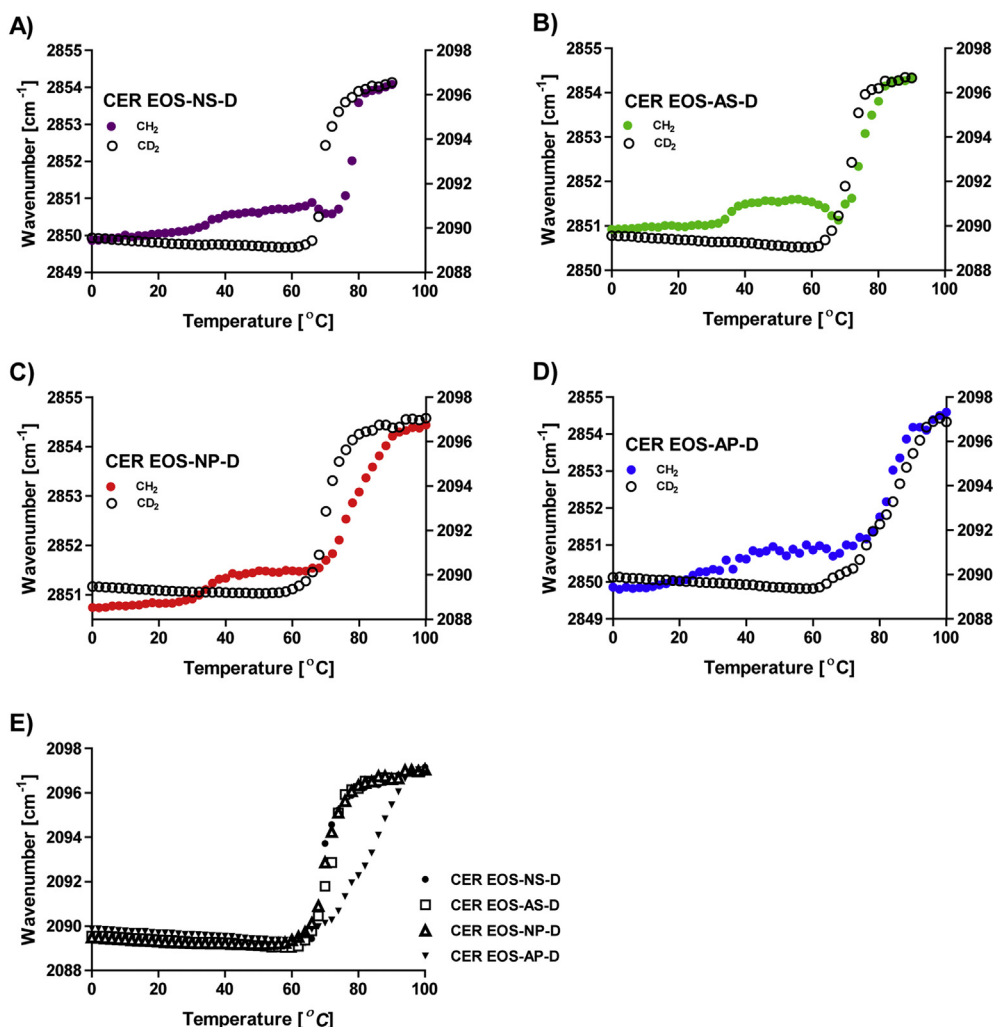
Fig. 5. Thermotropic response of the $\nu_s CH_2$ and $\nu_s CD_2$ modes of the lipid models. A–D) The CH_2 (filled circle) and the CD_2 (open circle) peak positions are plotted on the primary y-axis and secondary y-axis respectively displaying the phase transition temperatures of the CER and DFFA chains in the lipid models. E) $\nu_s CD_2$ modes of the lipid models showing the transition of the DFFA chains.

investigate the hydrogen bonding in the headgroup regions, the CER amide I ($\sim 1650\,cm^{-1}$) and amide II ($\sim 1550\,cm^{-1}$) were examined by FTIR. The CER amide I band is related mainly to the C═O stretching vibration while amide II results primarily from the N−H bending vibration and the C−N stretching vibration. Lower amide I and higher amide II frequencies are consistent with stronger hydrogen bonding [58,59]. The 1525–1675 cm^{-1} spectral region for the lipid models at 10 °C are displayed in Fig. 7. Regarding amide I frequencies, CER EOS-NS amide I mode are split into two components centred at 1624.6 cm^{-1} and 1641.1 cm^{-1}, attributed to intermolecular hydrogen bonding between two CER NS headgroups, similarly as reported in previous CER NS containing samples [59]. CER EOS-AS amide I mode shows an asymmetric peak centred at 1618.7 cm^{-1} and shoulder at 1633.8 cm^{-1}. As a non-hydroxy and an α-hydroxy sphingosine-based CER are present in this mixture, both may contribute to the signal. In the spectrum of CER-EOS-NP in which two non-hydroxy CERs contribute to the amide 1 band, the mode is a doublet with a sharp peak positioned at 1639.6 cm^{-1} and a broad shoulder on the left-hand side, positioned at 1618.8 cm^{-1} being consistent with earlier reports [60]. Finally, in the spectrum of the CER EOS-AP, only one broad band at an amide I frequency of 1624.2 cm^{-1} is present, which indicates the existence of strong hydrogen bonding interactions. The amide II bands are less complex. The single peaks are located at 1547.8 cm^{-1}, 1539.0 cm^{-1}, 1541.8 cm^{-1} and 1551.3 cm^{-1} in the spectrum of the CER EOS-NS,

CER EOS-AS, CER-EOS-NP, and CER EOS-AP respectively. CER EOS-AP displayed a comparatively low amide I frequency and the highest amide II frequency indicating stronger hydrogen bonding compared to the other models.

3.7. CER headgroup affects the lamellar organization in the lipid models

The lamellar organization in the lipid models was examined by SAXD. This technique can provide information about the lamellar phases including their repeat distances. The X-ray diffraction profiles of the various models are provided in Fig. 8. CER EOS-NS and CER EOS-AS had similar diffraction curves with 4 diffraction peaks attributed to LPP with a repeat distance of 12.5 and 12.6 nm respectively. When focusing on the CER EOS-NP, the lipids also assembled in the LPP as is indicated by the 6 diffraction orders with a repeat distance of 13.3 nm. Besides the LPP, the peak at 3.7 nm ($q = 1.69\,nm^{-1}$) indicates the presence of phase separated crystalline CER NP [61]. Finally, at $q = 1.1\,nm^{-1}$ (5.7 nm) a peak is present and no higher diffraction order could be identified. Consequently, this peak could not be assigned to a particular phase. Meanwhile, the diffraction pattern of CER EOS-AP model displayed 6 diffraction orders attributed to the LPP with a repeat distance of 13.4 nm. However, the 2nd and 3rd order peaks show a shoulder, indicating additional phases. The strong shoulder at the 3rd order peak is most probably the reason why the intensity of this order diffraction
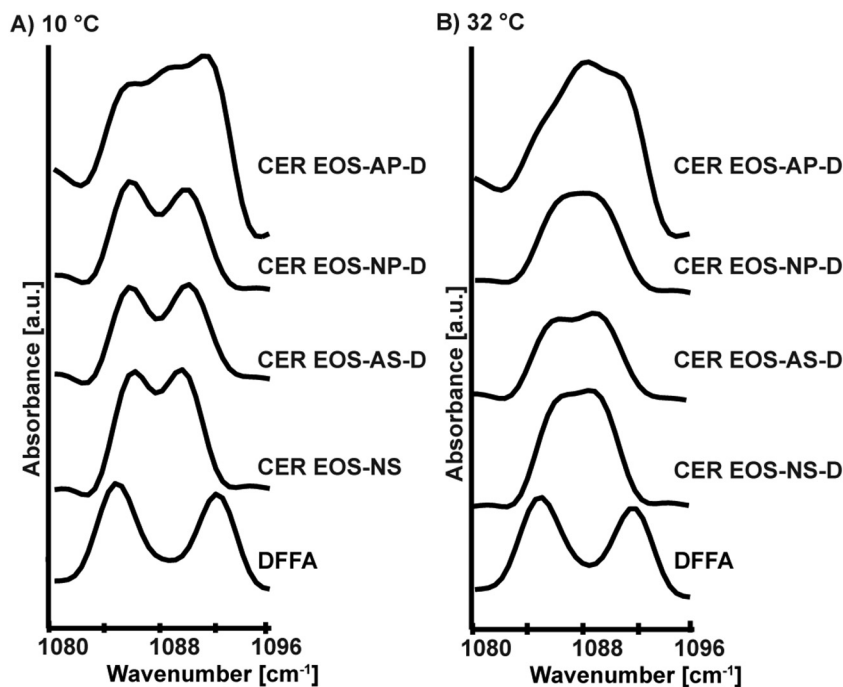
L.E. Uche, et al.   BBA - Biomembranes 1861 (2019) 1317–1328

Fig. 6. δCD$_2$ modes of the lipid models and DFFA. A) The δCD$_2$ curves of the various lipid models at 10 °C displaying reduced splitting compared to DFFA. B) The δCD$_2$ modes of the various models and DFFA at skin physiological temperature (32 °C).
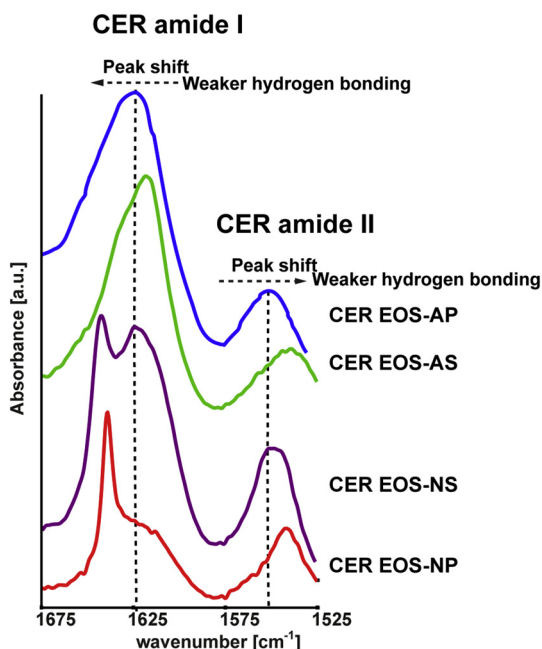

Fig. 7. IR spectrum of the 1525–1675 cm^{-1} region of the lipid models at 10 °C. CER EOS-NS amide I mode is split into 2 components. CER EOS-AS and CER EOS-NP amide I mode consist of a peak and a shoulder respectively, while CER EOS-AP amide I mode is not split. CER EOS-AP spectrum shows a comparatively low amide I frequency and the highest amide II frequency value indicating the strongest hydrogen bonding.

peak is somewhat higher in this diffraction profile compared with the 3rd order peak intensity in the pattern of the other systems. Similar to CER EOS-NP, an additional peak of 5.4 nm was detected. All SAXD profiles revealed the presence of a peak related to a spacing of 3.4 nm attributed to crystalline domains of phase separated CHOL. In summary, in all systems, the LPP was formed. In the sphingosine-based CER models besides the LPP, only phase separated CHOL was present. In

contrast, phytosphingosine-based systems formed the LPP, phase separated CHOL and additional phases.
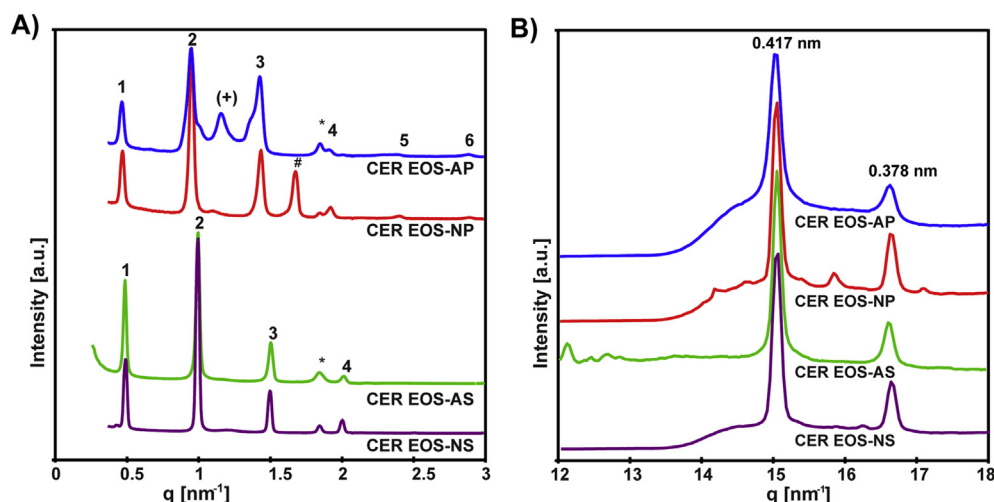
Besides the SAXD studies, the WAXD pattern of the models was measured to obtain information on the lateral packing of the lipid chains. The WAXD profiles are shown in Fig. 8B. All the models display two reflections, ~0.417 and 0.378 nm located at q = ~15.20 and 16.7 nm^{-1} respectively. While the 0.417 nm peak can be attributed to the orthorhombic and hexagonal packing, the 0.378 nm peak is only attributed to the orthorhombic packing. CER EOS-AP has the lowest intensity 0.378 nm peak indicating the smallest proportion of lipids forming an orthorhombic phase. These findings are in agreement with our FTIR result.

4. Discussion

4.1. CER headgroup affects the skin barrier function

The composition and organization of intercellular lipids of the SC are important for the skin barrier function. Changes in SC lipid composition have been reported in several inflammatory skin diseases [26,62–64], as well as in human skin equivalents [65,66] and regenerated SC after tape-stripping [67]. In these examples, the levels of CER AS and CER NS were increased at the expense of the level of CER NP. The exchange of CER subclasses contributed to a compromised skin barrier, as illustrated by increased values of transepidermal water loss (TEWL) [62]. However, studying whether a change in the ratio between these lipid classes is an underlying factor for an impaired barrier function is not possible in intact SC as there are always other associated changes in the lipid or protein composition, and lipids cannot be extracted selectively from SC. Therefore to study the relationship between lipid composition, lipid organization and barrier function, lipid model membranes were developed [42,68].

The aim of the present study was to examine the effect of CER headgroup architecture, particularly focusing on the comparison between sphingosine and phytosphingosine-based CER compositions, on the permeability and phase behavior of lipid models. Lipid model systems of an equimolar mixture of CERs, CHOL and FFAs were employed,

Fig. 8. X-ray diffraction profile of the hydrated lipid models. A) The SAXD profile of the lipid models. The arabic numbers 1, 2, 3 indicate the diffraction orders of the LPP. In the diffraction profile of CER EOS-NS, a series of diffraction peaks positioned at $q = 0.50$. 1.00, 1.51, 2.01 nm^{-1} indicate the 1st, 2nd, 3rd and 4th diffraction orders attributed to the LPP with a repeat distance of 12.5 nm. In the diffraction profile of CER EOS-AS, the peak positions at $q = 0.49$, 0.99, 1.52 and 1.98 nm^{-1} indicate the 1st, 2nd, 3rd and 4th diffraction orders attributed to the LPP with a repeat distance of 12.6 nm. In the diffraction pattern of CER EOS-NP, the peak positions at $q = 0.48$, 0.96, 1.45, 1.94 (a shoulder) 2.41 and 2.90 nm^{-1} are attributed to 1st, 2nd, 3rd, 4th, 5th and 6th diffraction orders of the LPP with a repeat distance of 13.3 nm. The reflection denoting crystalline CER NP is indicated by #. In the diffraction pattern of CER EOS-AP, the reflections at $q = 0.47$, 0.96, 1.43, 1.93 (a shoulder), 2.40, 2.89 nm^{-1} are attributed to the 1st, 2nd, 3rd, 4th, 5th and 6th diffraction orders attributed to the LPP with a repeat distance of 13.4 nm. The reflections at $q = 1.12$ nm^{-1} in CER EOS-NP and 1.16 nm^{-1} in CER EOS-AP are indicated by (+) and represent an unknown phase. The peaks attributed to crystalline CHOL are indicated by asterisk *. B) WAXD profile of the lipid models displaying two peaks, the 0.417 and the 0.378 nm peaks, located at $q = \sim 15.2$ and 16.7 nm^{-1} respectively. CER EOS-AP showed the lowest intensity 0.378 nm peak, indicating the lowest proportion of orthorhombic phase.

in a similar molar ratio as is present in human SC [10]. The CER fraction of the lipid mixture comprised of 60% of either CER NS, AS, NP or AP with a single chain length and 40% CER EOS in order to form an LPP model system. Our purpose was to study primarily the formation of the LPP. To form only a single LPP structure and avoid the formation of the SPP, the CER EOS level was increased beyond the approximate 10 mol% reported in the human SC [27]. Our results demonstrate that membranes containing CERs with the phytosphingosine subclass exhibited a stronger lipid barrier. These findings indicate that increased levels of CER NS and reduced level of CER NP as observed in atopic dermatitis patients [69], psoriatic scale [47] and compromised tape-stripped skin [67] may contribute to the impaired barrier function. In contrast, it was previously shown that CER NP encouraged higher permeability through the model membrane when compared to CER NS [43]. In that study, no CER EOS was incorporated in the mixtures, thus, the lipids assembled in the SPP rather than the LPP as in the present study. Furthermore, we observed that CER EOS enhances the miscibility between the different lipid components (unpublished results), which may explain the difference in result. In another study, no difference in permeability was observed between model membranes of the same FFA composition containing either CER NS or a CER mixture incorporating sphingosine and phytosphingosine CERs [45]. However, this difference may be due to i) a lower concentration of phytosphingosine CERs that was replaced by the sphingosine counterpart in the CER mixture, ii) a simultaneous change in CER chain length distribution, in which CERs with C16 acyl chain were replaced by CERs with a C24 acyl chain in the present study and iii) the absence of CER EOS. The CER NS model membrane in that study, despite lacking CER EOS, resulted in an *E*-PABA flux value similar to that of CER EOS-NS model in the current study. However, as these are different experiments and small differences in temperature of the membranes substantially affect the flux [45], this may play a role. Furthermore, although low levels of CER EOS may reduce the permeability, high levels of CER EOS may affect the flux in a different way due to a higher level of liquid domains [37].

When comparing the E-PABA flux of lipid models prepared with non-hydroxy fatty acid-based CERs to the models prepared with α-hydroxy fatty acid-based CERs with the same sphingoid base (e.g. CER NS and AS), there was no significant difference in permeability. The phytosphingosine CERs which resulted in significantly lower membrane permeability do not possess a 4,5 trans double bond present in the sphingosine CERs but rather, contain an additional hydroxyl group on C4 position on the base chain. Thus, the position of the hydroxyl group

in the CER headgroup and probably the presence or absence of the trans-double bond influenced the permeability of the model membrane.

4.2. CER headgroup affects the lipid phase behavior, chain, and headgroup interactions in model SC

A wider ordered-disordered phase transition temperature range was observed in the phytosphingosine-based CER models. This may be due to either a combined effect of differences in headgroup interactions and/or the presence of the multiple phases. The CER headgroup did not have an effect on the domain size of the lipids forming an orthorhombic packing since all the models exhibited large interpeak distance approaching the maximum value, indicating large orthorhombic domain sizes at 10 °C. However, when comparing the intensities of the characteristic orthorhombic peaks, which relate directly to the proportion of the orthorhombic phase [70], CER EOS-AP exhibited the least proportion of lipids in an orthorhombic phase. This was confirmed by the wide-angle X-ray diffraction pattern of CER-EOS-AP. Our results are in agreement with a previous infrared study of ternary SC models reporting that phytosphingosine-based CERs adopt a hexagonal chain packing [71], while sphingosine-based CERs adopt an orthorhombic chain packing [33]. The higher fraction of lipids forming a hexagonal packing in CER EOS-AP may be due to a larger interfacial area per headgroup of the phytosphingosine CERs than the sphingosine analogues, which allows more space and optimal geometry for hydrogen bonding [72].

In previous studies, it has been observed that an increase in the fraction of lipids forming a hexagonal packing results in an increase in permeability [73]. On the contrary, CER EOS-AP, which contained the highest proportion of the hexagonal phase, resulted in the lowest permeability. Our study indicates strong hydrogen bonding within the CER EOS-AP model. In this particular case, the effect of increased hydrogen bonding in the headgroup region seems to overrule the reduced interchain van der Waals interactions resulting in a reduced permeability. A previous infrared study of individual CERs also reported stronger hydrogen bonding and hexagonal lateral packing in phytosphingosine CERs and weaker hydrogen bonding and orthorhombic packing in their analogous sphingosine CERs [60]. CER EOS-NP displayed a low amide II frequency and an orthorhombic lateral packing, which are characteristic of sphingosine CERs. This may be caused by the presence of 40% CER EOS that contributed to the molecular interactions observed in the models in the current study. In addition, the resilient

orthorhombic phase of CER EOS-NP evinced by its indisputably high $T_{M,OR-HEX}$, contributed to its low permeability.

Focusing on the mixing property of the lipid chains, CERs and DFFAs chains were mixed with each other in all models as indicated by the weak split in the δCD_2 modes of the models compared to the strong split in DFFA. The transition of the CER and FFA chain in CER EOS-NP does not occur in exactly the same temperature range. This may be due to the presence of CER and FFA rich regions within the orthorhombic lattice or to phase separated CER NP. Since recrystallization of only the CER chains occurred in CER-EOS-NS-D, the recrystallization observed in CER-EOS-NS δCH_2 mode was thus due to the CERs. It is also remarkable that a modification in CER-EOS-NS model, by spraying the lipid mixture at a lower concentration, of $< 5 \, mg/ml$ resulted in the disappearance of CER chain recrystallization (Fig. S5). Considering the $\nu_s CD_2$ modes, the DFFAs in the CER EOS-AP-D underwent an ordered-disordered phase transition at a higher temperature than in the other models implying of a stronger cohesive bond. This may be attributed to the stronger headgroup hydrogen bonding interaction in CER EOS-AP.

4.3. CER headgroup affect the lamellar organization in lipid model mixtures

In-depth knowledge of the lipid organization within the unit cell of the lamellar phases is important for understanding the skin barrier function. In the present study we observed that in all four systems an LPP can be formed, irrespective of the choice of CER NS, AS, NP or AP. However, in CER EOS-NS and CER EOS-AS systems, the LPP is formed without additional phases, except for phase separated crystalline CHOL. These results indicate that it is easier for CER EOS combined with CER NS or AS, to exclusively form the LPP than when combined with CER AP or NP. Furthermore, when forming the LPP, the characteristic intensity distribution of the 1st (weaker intensity), 2nd (stronger intensity) and 3rd (weaker intensity) order peak is observed (for additional information see Section 4.4), signifying that the LPP has been formed. The LPP in phytosphingosine-based CER models had longer periodicities than those of their sphingosine counterparts. In contrast, the non-hydroxy or α-hydroxy CER models with the same sphingoid base (e.g. CER NS and AS), did not show significant differences in their LPP repeat distance. Possible explanations for the longer repeat distance experienced by the phytosphingosine-based CER model are i) the presence of additional water molecules in the headgroup region that would cause swelling in the lamellar. However, this is unlikely as fully hydrated and dry mixtures result in similar repeat distance (Fig. S6); ii) the presence of additional phases. In the diffraction pattern of the CER EOS-NP, a strong reflection at $1.7 \, nm^{-1}$ is attributed to crystalline CER NP [61]. As a consequence, the LPP contained a higher proportion of CER EOS, which induced an increase in the periodicity (unpublished data). This would also explain the similarity in repeat distances of non-hydroxy and α-hydroxy based sphingoid bases, as in these models no additional phases had formed; iii) a difference in the headgroup orientation at the basal plane of the lamellar phase. This change in orientation may be related to the presence/absence of 4,5 trans double bond, number and position of hydroxyl groups in the CER species as is observed for the air-water interface [74] or iv) a difference in the arrangement of the CERs, namely, linear versus hairpin arrangement.

4.4. The formation of the LPP in SC and lipid mixtures

Using X-ray diffraction, the LPP has been identified not only in human SC [75] but also in murine [14,76], porcine skin [12] and human skin equivalents [65]. In all these cases, the repeat distance of the LPP was reported to be approximately 13 nm. By examining CERs isolated from porcine [31] or human SC [41], mixed with cholesterol and FFAs, both the LPP and SPP were reproduced all with repeat distance very similar to that in native SC. In subsequent studies, synthetic CERs were used as this allowed a more detailed analysis of the interactions between the individual lipids. It was reported that after

incorporating acyl CERs in the synthetic CER mixtures, the lipids assembled in the LPP and SPP, although the repeat distance of the LPP was somewhat shorter [36]. This could be expected as the chain lengths of the natural lipids are longer than those of the synthetic CERs: the mean total CER chain length (sphingoid base + acyl chain) in SC of human skin is approximately 47C atoms [77], while in the lipid model system used in these studies the CERs have a mean chain length of 45.2C atoms (calculated from the CER subclass composition) [36]. In addition, the choice of the headgroup may also contribute to a difference in repeat distance, as is reported in the present paper. Therefore, differences in lamellar repeat distance in synthetic mixtures compared to that in native SC can be explained without assuming different lipid arrangements in the unit cell as was suggested recently [78]. In fact the similarity in the lipid arrangement in the LPP in mixtures prepared from synthetic [36], and isolated CERs [69,79], but also in SC of mice skin [76] and human skin equivalents [65] (In both SC, the lipids form primarily an LPP) has been demonstrated by the characteristic intensity distribution of the various diffraction peaks attributed to the LPP: the 1st and 3rd order diffraction peaks have a lower intensity than the 2nd order diffraction peak. This intensity distribution is a reflection of the electron density profile in the unit cell of a lamellar phase. Therefore, all these systems do have a similar unit cell electron density profile, and thus the arrangement of the lipids appears to be very similar. The latter has also been demonstrated by the similarity in the structure factors of the LPP in SC and those of the LPP in synthetic and isolated CER mixtures [49]. These structure factors are the basis for calculating the electron density profile of the unit cell.

It is important to realize, especially when using synthetic CERs, after the proper composition, the choice of the spraying method and the temperature of annealing are both crucial for the LPP formation, which has been discussed previously [78]. Setting the equilibration temperature too high or too low can be detrimental for the LPP formation [80]. Furthermore, the distance between the nozzle and the spraying surface, and the gas flow are crucial parameters. Differences in the choice of these parameters may be a reason why phases with the characteristic LPP intensity distribution are sometimes not formed even with a proper choice of the CER composition [46], while a very similar lipid composition does result in the exclusive formation of the LPP [48]. In contrast, to current literature [78], an increase in the level of CER EOS results in an increase in the fraction of lipids forming the LPP at the expense of the lipids forming the SPP, keeping the characteristic intensity distribution of diffraction peaks of the LPP very similar [38,48]. As the intensity distribution is directly related to the electron density profile, this demonstrates that by increasing the CER EOS level, there is no substantial change in the LPP electron density profile and therefore the basic structure in the unit cell remains the same. Finally, the absence of the LPP in systems in which the CER EOS is replaced by a CER EOS with a saturated but branched C18-acyl chain is most likely due to a reduction of a fluid phase as has been shown by NMR studies [81]. This is in agreement with a previous publication demonstrating that the presence of a fluid phase is an absolute necessity for the formation of the LPP [82].

5. Conclusion

CER headgroup architecture influences the permeability, lipid phase behavior and molecular interactions of lipid models. In the presence of CER EOS, the majority of lipid population in all the models assembled in the LPP. When focusing on the interactions in the systems, we have shown that due to distinct phase behavior, lipid chain packing and headgroup interactions, sphingosine-based CER model membranes resulted in a higher permeability than the phytosphingosine-based models. This is an important observation for understanding the effect of changes in CER subclass composition on the skin barrier function in diseased skin, which is paramount to the optimization and targeting of therapies.

Transparency document

The Transparency document associated with this article can be found, in online version.

Acknowledgements

We thank the company Evonik for the donation of CERs. We also acknowledge the staff at the DUBBLE beamline 26b at the ESRF, Grenoble, France who assisted with the X-ray diffractions measurements.

Appendix A. Supplementary data

Supplementary data to this article can be found online at https://doi.org/10.1016/j.bbamem.2019.04.005.

References

[1] I.H. Blank, Cutaneous barriers, J. Invest. Dermatol. 45 (1965) 249–256.
[2] K.C. Madison, Barrier function of the skin: "la raison d'etre" of the epidermis, J. Invest. Dermatol. 121 (2003) 231–241.
[3] K.R. Feingold, Thematic review series: skin lipids. The role of epidermal lipids in cutaneous permeability barrier homeostasis, J. Lipid Res. 48 (2007) 2531–2546.
[4] P.M. Elias, Epidermal barrier function - intercellular lamellar lipid structures, origin, composition and metabolism, J. Control. Release 15 (1991) 199–208.
[5] P.S. Talreja, N.K. Kleene, W.L. Pickens, T.F. Wang, G.B. Kasting, Visualization of the lipid barrier and measurement of lipid pathlength in human stratum corneum, AAPS Pharmsci., 3 (2001) art. no. 13.
[6] H.E. Bodde, M.A.M. Kruithof, J. Brussee, H.K. Koerten, Visualization of normal and enhanced Hgcl2 transport through human-skin invitro, Int. J. Pharm. 53 (1989) 13–24.
[7] G.M. Gray, H.J. Yardley, Lipid compositions of cells isolated from pig, human, and rat epidermis, J. Lipid Res. 16 (1975) 434–440.
[8] P.M. Elias, J. Goerke, D.S. Friend, Mammalian epidermal barrier layer lipids: composition and influence on structure, J. Invest. Dermatol. 69 (1977) 535–546.
[9] P.M. Elias, Epidermal lipids, membranes, and keratinization, Int. J. Dermatol. 20 (1981) 1–19.
[10] A. Weerheim, M. Ponec, Determination of stratum corneum lipid profile by tape stripping in combination with high-performance thin-layer chromatography, Arch. Dermatol. Res. 293 (2001) 191–199.
[11] P.W. Wertz, B. van den Bergh, The physical, chemical and functional properties of lipids in the skin and other biological barriers, Chem. Phys. Lipids 91 (1998) 85–96.
[12] J.A. Bouwstra, G.S. Gooris, W. Bras, D.T. Downing, Lipid organization in pig stratum-corneum, J. Lipid Res. 36 (1995) 685–695.
[13] J.R. Hill, P.W. Wertz, Molecular models of the intercellular lipid lamellae from epidermal stratum corneum, Biochim. Biophys. Acta 1616 (2003) 121–126.
[14] S.H. White, D. Mirejovsky, G.I. King, Structure of lamellar lipid domains and corneocyte envelopes of murine stratum corneum. An X-ray diffraction study, Biochemistry 27 (1988) 3725–3732.
[15] F. Damien, M. Boncheva, The extent of orthorhombic lipid phases in the stratum corneum determines the barrier efficiency of human skin in vivo, J. Invest. Dermatol. 130 (2010) 611–614.
[16] M. Boncheva, F. Damien, V. Normand, Molecular organization of the lipid matrix in intact stratum corneum using ATR-FTIR spectroscopy, Biochim. Biophys. Acta 1778 (2008) 1344–1355.
[17] D.J. Moore, M.E. Rerek, R. Mendelsohn, Lipid domains and orthorhombic phases in model stratum corneum: evidence from Fourier transform infrared spectroscopy studies, Biochem. Biophys. Res. Commun. 231 (1997) 797–801.
[18] R. Mendelsohn, M.E. Rerek, D.J. Moore, Infrared spectroscopy and microscopic imaging of stratum corneum models and skin, Phys. Chem. Chem. Phys. 2 (2000) 4651–4657.
[19] D. Groen, D.S. Poole, G.S. Gooris, J.A. Bouwstra, Is an orthorhombic lateral packing and a proper lamellar organization important for the skin barrier function? Biochim. Biophys. Acta 1808 (2011) 1529–1537.
[20] K.J. Robson, M.E. Stewart, S. Michelsen, N.D. Lazo, D.T. Downing, 6-Hydroxy-4-sphingenine in human epidermal ceramides, J. Lipid Res. 35 (1994) 2060–2068.
[21] M.E. Stewart, D.T. Downing, A new 6-hydroxy-4-sphingenine-containing ceramide in human skin, J. Lipid Res. 40 (1999) 1434–1439.
[22] Y. Masukawa, H. Narita, E. Shimizu, N. Kondo, Y. Sugai, T. Oba, R. Homma, J. Ishikawa, Y. Takagi, T. Kitahara, Y. Takema, K. Kita, Characterization of overall ceramide species in human stratum corneum, J. Lipid Res. 49 (2008) 1466–1476.
[23] J. van Smeden, L. Hoppel, R. van der Heijden, T. Hankemeier, R.J. Vreeken, J.A. Bouwstra, LC/MS analysis of stratum corneum lipids: ceramide profiling and discovery, J. Lipid Res. 52 (2011) 1211–1221.
[24] M. Rabionet, K. Gorgas, R. Sandhoff, Ceramide synthesis in the epidermis, Biochim. Biophys. Acta 1841 (2014) 422–434.
[25] P.W. Wertz, M.C. Miethke, S.A. Long, J.S. Strauss, D.T. Downing, The composition of the ceramides from human stratum-corneum and from comedones, J. Invest. Dermatol. 84 (1985) 410–412.
[26] J. van Smeden, J.A. Bouwstra, Stratum Corneum lipids: their role for the skin barrier function in healthy subjects and atopic dermatitis patients, Curr. Probl. Dermatol. 49 (2016) 8–26.
[27] R. t'Kindt, L. Jorge, E. Dumont, P. Couturon, F. David, P. Sandra, K. Sandra, Profiling and characterizing skin ceramides using reversed-phase liquid chromatography–quadrupole time-of-flight mass spectrometry, Anal. Chem. 84 (2012) 403–411.
[28] G.S. Gooris, J.A. Bouwstra, Infrared spectroscopic study of stratum corneum model membranes prepared from human ceramides, cholesterol, and fatty acids, Biophys. J. 92 (2007) 2785–2795.
[29] J. Caussin, G.S. Gooris, M. Janssens, J.A. Bouwstra, Lipid organization in human and porcine stratum corneum differs widely, while lipid mixtures with porcine ceramides model human stratum corneum lipid organization very closely, Biochim. Biophys. Acta 1778 (2008) 1472–1482.
[30] T.J. McIntosh, M.E. Stewart, D.T. Downing, X-ray diffraction analysis of isolated skin lipids: reconstitution of intercellular lipid domains, Biochemistry 35 (1996) 3649–3653.
[31] J.A. Bouwstra, G.S. Gooris, K. Cheng, A. Weerheim, W. Bras, M. Ponec, Phase behavior of isolated skin lipids, J. Lipid Res. 37 (1996) 999–1011.
[32] J.A. Bouwstra, G.S. Gooris, F.E. Dubbelaar, M. Ponec, Phase behavior of stratum corneum lipid mixtures based on human ceramides: the role of natural and synthetic ceramide 1, J. Invest. Dermatol. 118 (2002) 606–617.
[33] D.J. Moore, M.E. Rerek, Insights into the molecular organization of lipids in the skin barrier from infrared spectroscopy studies of stratum corneum lipid models, Acta Derm-Venereol. (2000) 16–22.
[34] M. Lafleur, Phase behaviour of model stratum corneum lipid mixtures: an infrared spectroscopy investigation, Can. J. Chem. 76 (1998) 1501–1511.
[35] J. Thewalt, N. Kitson, C. Araujo, A. Mackay, M. Bloom, Models of stratum-corneum intercellular membranes — the sphingolipid headgroup is a determinant of phase-behavior in mixed lipid dispersions, Biochim. Bioph. Res. Co. 188 (1992) 1247–1252.
[36] M.W. de Jager, G.S. Gooris, M. Ponec, J.A. Bouwstra, Lipid mixtures prepared with well-defined synthetic ceramides closely mimic the unique stratum corneum lipid phase behavior, J. Lipid Res. 46 (2005) 2649–2656.
[37] M. Janssens, G.S. Gooris, J.A. Bouwstra, Infrared spectroscopy studies of mixtures prepared with synthetic ceramides varying in head group architecture: coexistence of liquid and crystalline phases, Biochim. Biophys. Acta 1788 (2009) 732–742.
[38] M. de Jager, G. Gooris, M. Ponec, J. Bouwstra, Acylceramide head group architecture affects lipid organization in synthetic ceramide mixtures, J. Invest. Dermatol. 123 (2004) 911–916.
[39] J.A. Bouwstra, G.S. Gooris, F.E. Dubbelaar, A.M. Weerheim, A.P. Ijzerman, M. Ponec, Role of ceramide 1 in the molecular organization of the stratum corneum lipids, J. Lipid Res. 39 (1998) 186–196.
[40] D. Groen, G.S. Gooris, J.A. Bouwstra, Model membranes prepared with ceramide EOS, cholesterol and free fatty acids form a unique lamellar phase, Langmuir 26 (2010) 4168–4175.
[41] J.A. Bouwstra, G.S. Gooris, F.E. Dubbelaar, M. Ponec, Phase behavior of lipid mixtures based on human ceramides: coexistence of crystalline and liquid phases, J. Lipid Res. 42 (2001) 1759–1770.
[42] M. de Jager, W. Groenink, R. Bielsa i Guivernau, E. Andersson, N. Angelova, M. Ponec, J. Bouwstra, A novel in vitro percutaneous penetration model: evaluation of barrier properties with p-aminobenzoic acid and two of its derivatives, Pharm. Res. 23 (2006) 951–960.
[43] B. Skolova, A. Kovacik, O. Tesar, L. Opalka, K. Vavrova, Phytosphingosine, sphingosine and dihydrosphingosine ceramides in model skin lipid membranes: permeability and biophysics, Biochim. Biophys. Acta 1859 (2017) 824–834.
[44] B. Skolova, K. Jandovska, P. Pullmannova, O. Tesar, J. Roh, A. Hrabalek, K. Vavrova, The role of the trans double bond in skin barrier sphingolipids: permeability and infrared spectroscopic study of model ceramide and dihydroceramide membranes, Langmuir 30 (2014) 5527–5535.
[45] M. Uchiyama, M. Oguri, E.H. Mojumdar, G.S. Gooris, J.A. Bouwstra, Free fatty acids chain length distribution affects the permeability of skin lipid model membranes, Biochim. Biophys. Acta 1858 (2016) 2050–2059.
[46] L. Opalka, A. Kovacik, J. Maixner, K. Vavrova, Omega-O-Acylceramides in skin lipid membranes: effects of concentration, sphingoid base, and model complexity on microstructure and permeability, Langmuir 32 (2016) 12894–12904.
[47] S. Motta, M. Monti, S. Sesana, R. Caputo, S. Carelli, R. Ghidoni, Ceramide composition of the psoriatic scale, Biochim. Biophys. Acta 1182 (1993) 147–151.
[48] G.S. Gooris, M. Kamran, A. Kros, D.J. Moore, J.A. Bouwstra, Interactions of dipalmitoylphosphatidylcholine with ceramide-based mixtures, Biochim. Biophys. Acta 1860 (2018) 1272–1281.
[49] D. Groen, G.S. Gooris, J.A. Bouwstra, New insights into the stratum corneum lipid organization by X-ray diffraction analysis, Biophys. J. 97 (2009) 2242–2249.
[50] P.W.W.a.D.T. Downing, Physiology, Biochemistry and Molecular Biology of the skin, in, vol. 1, Oxford University Press, New York, 1991, pp. 205–236.
[51] International Conference on Harmonization (ICH) Q2 (R1), Validation of Analytical Procedures, Text and Methodology, Geneva, 2005.
[52] European Pharmacopoeia. 8 ed., European directorate for the quality of medicines & healthcare, Strasbourg, 2014.
[53] M. Oguri, G.S. Gooris, K. Bito, J.A. Bouwstra, The effect of the chain length distribution of free fatty acids on the mixing properties of stratum corneum model membranes, Biochim. Biophys. Acta 1838 (2014) 1851–1861.
[54] R. Mendelsohn, D.J. Moore, Infrared determination of conformational order and phase behavior in ceramides and stratum corneum models, Methods Enzymol. 312 (2000) 228–247.
[55] R.G. Snyder, M.C. Goh, V.J.P. Srivatsavoy, H.L. Strauss, D.L. Dorset, Measurement

of the growth-kinetics of microdomains in binary N-alkane solid-solutions by infrared-spectroscopy, J. Phys. Chem-US 96 (1992) 10008–10019.

[56] R. Mendelsohn, G.L. Liang, H.L. Strauss, R.G. Snyder, IR spectroscopic determination of gel state miscibility in long-chain phosphatidylcholine mixtures, Biophys. J. 69 (1995) 1987–1998.

[57] I. Pascher, Molecular arrangements in sphingolipids. Conformation and hydrogen bonding of ceramide and their implication on membrane stability and permeability, Biochim. Biophys. Acta 455 (1976) 433–451.

[58] D.J. Moore, M.E. Rerek, R. Mendelsohn, FTIR spectroscopy studies of the conformational order and phase behavior of ceramides, J. Phys. Chem-US 101 (1997) 8933–8940.

[59] D.J. Moore, M.E. Rerek, R. Mendelsohn, Role of ceramides 2 and 5 in the structure of the stratum corneum lipid barrier, Int. J. Cosmet. Sci. 21 (1999) 353–368.

[60] M.E. Rerek, H.C. Chen, B. Markovic, D. Van Wyck, P. Garidel, R. Mendelsohn, D.J. Moore, Phytosphingosine and sphingosine ceramide headgroup hydrogen bonding: structural insights through thermotropic hydrogen/deuterium exchange, J. Phys. Chem-US 105 (2001) 9355–9362.

[61] M.W. de Jager, G.S. Gooris, I.P. Dolbnya, M. Ponec, J.A. Bouwstra, Modelling the stratum corneum lipid organisation with synthetic lipid mixtures: the importance of synthetic ceramide composition, Biochim. Biophys. Acta 1664 (2004) 132–140.

[62] J. Ishikawa, H. Narita, N. Kondo, M. Hotta, Y. Takagi, Y. Masukawa, T. Kitahara, Y. Takema, S. Koyano, S. Yamazaki, A. Hatamochi, Changes in the ceramide profile of atopic dermatitis patients, J. Invest. Dermatol. 130 (2010) 2511–2514.

[63] M. Danso, W. Boiten, V. van Drongelen, K. Gmelig Meijling, G. Gooris, A. El Ghalbzouri, S. Absalah, R. Vreeken, S. Kezic, J. van Smeden, S. Lavrijsen, J. Bouwstra, Altered expression of epidermal lipid bio-synthesis enzymes in atopic dermatitis skin is accompanied by changes in stratum corneum lipid composition, J. Dermatol. Sci. 88 (2017) 57–66.

[64] A. Di Nardo, P. Wertz, A. Giannetti, S. Seidenari, Ceramide and cholesterol composition of the skin of patients with atopic dermatitis, Acta Derm-Venereol. 78 (1998) 27–30.

[65] V.S. Thakoersing, G.S. Gooris, A. Mulder, M. Rietveld, A. El Ghalbzouri, J.A. Bouwstra, Unraveling barrier properties of three different in-house human skin equivalents, Tissue Eng. Pt. C-Me. 18 (2012) 1–11.

[66] M.O. Danso, V. van Drongelen, A. Mulder, J. van Esch, H. Scott, J. van Smeden, A. El Ghalbzouri, J.A. Bouwstra, TNF-alpha and Th2 cytokines induce atopic dermatitis-like features on epidermal differentiation proteins and stratum corneum lipids in human skin equivalents, J. Invest. Dermatol. 134 (2014) 1941–1950.

[67] W.A. Boiten, T. Berkers, S. Absalah, J. van Smeden, A.P.M. Lavrijsen, J.A. Bouwstra, Applying a vernix caseosa based formulation accelerates skin barrier repair by modulating lipid biosynthesis, J. Lipid Res. 59 (2018) 250–260.

[68] M. de Jager, W. Groenink, J. van der Spek, C. Janmaat, G. Gooris, M. Ponec, J. Bouwstra, Preparation and characterization of a stratum corneum substitute for in vitro percutaneous penetration studies, Biochim. Biophys. Acta 1758 (2006) 636–644.

[69] M. Janssens, J. van Smeden, G.S. Gooris, W. Bras, G. Portale, P.J. Caspers, R.J. Vreeken, S. Kezic, A.P. Lavrijsen, J.A. Bouwstra, Lamellar lipid organization and ceramide composition in the stratum corneum of patients with atopic eczema, J. Invest. Dermatol. 131 (2011) 2136–2138.

[70] T. Berkers, L. van Dijk, S. Absalah, J. van Smeden, J.A. Bouwstra, Topically applied fatty acids are elongated before incorporation in the stratum corneum lipid matrix in compromised skin, Exp. Dermatol. 26 (2017) 36–43.

[71] M.E. Rerek, D. Van Wyck, R. Mendelsohn, D.J. Moore, FTIR spectroscopic studies of lipid dynamics in phytosphingosine ceramide models of the stratum corneum lipid matrix, Chem. Phys. Lipids 134 (2005) 51–58.

[72] B.M. Lunden, H. Lofgren, I. Pascher, Accommodation of hydroxyl groups and their hydrogen bond system in a hydrocarbon matrix, Chem. Phys. Lipids 20 (1977) 263–271.

[73] E.H. Mojumdar, R.W. Helder, G.S. Gooris, J.A. Bouwstra, Monounsaturated fatty acids reduce the barrier of stratum corneum lipid membranes by enhancing the formation of a hexagonal lateral packing, Langmuir 30 (2014) 6534–6543.

[74] H. Lofgren, I. Pascher, Molecular arrangements of sphingolipids. The monolayer behaviour of ceramides, Chem. Phys. Lipids 20 (1977) 273–284.

[75] J.A. Bouwstra, G.S. Gooris, J.A. Vanderspek, W. Bras, Structural investigations of human stratum-corneum by small-angle X-ray-scattering, J. Invest. Dermatol. 97 (1991) 1005–1012.

[76] J.A. Bouwstra, G.S. Gooris, J.A. van der Spek, S. Lavrijsen, W. Bras, The lipid and protein structure of mouse stratum corneum: a wide and small angle diffraction study, Biochim. Biophys. Acta 1212 (1994) 183–192.

[77] M. Janssens, J. van Smeden, G.S. Gooris, W. Bras, G. Portale, P.J. Caspers, R.J. Vreeken, T. Hankemeier, S. Kezic, R. Wolterbeek, A.P. Lavrijsen, J.A. Bouwstra, Increase in short-chain ceramides correlates with an altered lipid organization and decreased barrier function in atopic eczema patients, J. Lipid Res. 53 (2012) 2755–2766.

[78] T. Schmitt, S. Lange, S. Sonnenberger, B. Dobner, A. Deme, A. Langner, R.H.H. Neubert, The long periodicity phase (LPP) controversy part I: the influence of a natural-like ratio of the CER[EOS] analogue [EOS]-br in a CER[NP]/[AP] based stratum corneum modelling system: a neutron diffraction study, Biochim. Biophys. Acta 1861 (2019) 306–315.

[79] J.A. Bouwstra, G.S. Gorris, K. Cheng, A. Weerheim, W. Bras, M. Ponec, Phase behavior of isolated skin lipids, J. Lipid Res. 37 (1996) 999–1011.

[80] M.W. de Jager, G.S. Gooris, I.P. Dolbnya, W. Bras, M. Ponec, J.A. Bouwstra, Novel lipid mixtures based on synthetic ceramides reproduce the unique stratum corneum lipid organization, J. Lipid Res. 45 (2004) 923–932.

[81] A. Eichner, S. Stahlberg, S. Sonnenberger, S. Lange, B. Dobner, A. Ostermann, T.E. Schrader, T. Hauss, A. Schroeter, D. Huster, R.H.H. Neubert, Influence of the penetration enhancer isopropyl myristate on stratum corneum lipid model membranes revealed by neutron diffraction and H-2 NMR experiments, Biochim. Biophys. Acta 1859 (2017) 745–755.

[82] J.A. Bouwstra, G.S. Gooris, F.E.R. Dubbelaar, M. Ponec, Phase behavior of stratum corneum lipid mixtures based on human ceramides: the role of natural and synthetic ceramide 1, J. Invest. Dermatol. 118 (2002) 606–617.